EFFECTS OF SPACE ENVIRONMENT
ON LEO SATELLITE DRAG

Timothy Kodikara[1,2], Brett Carter[1],
Robert Norman[1,2] and Kefei Zhang[1,2]

[1]The SPACE Research Centre, RMIT University, GPO Box 2476V, Australia
[2]SERC Limited, AITC2 Mount Stromlo Observatory, ACT 2611, Australia
Correspondence: timothy.kodikara@rmit.edu.au

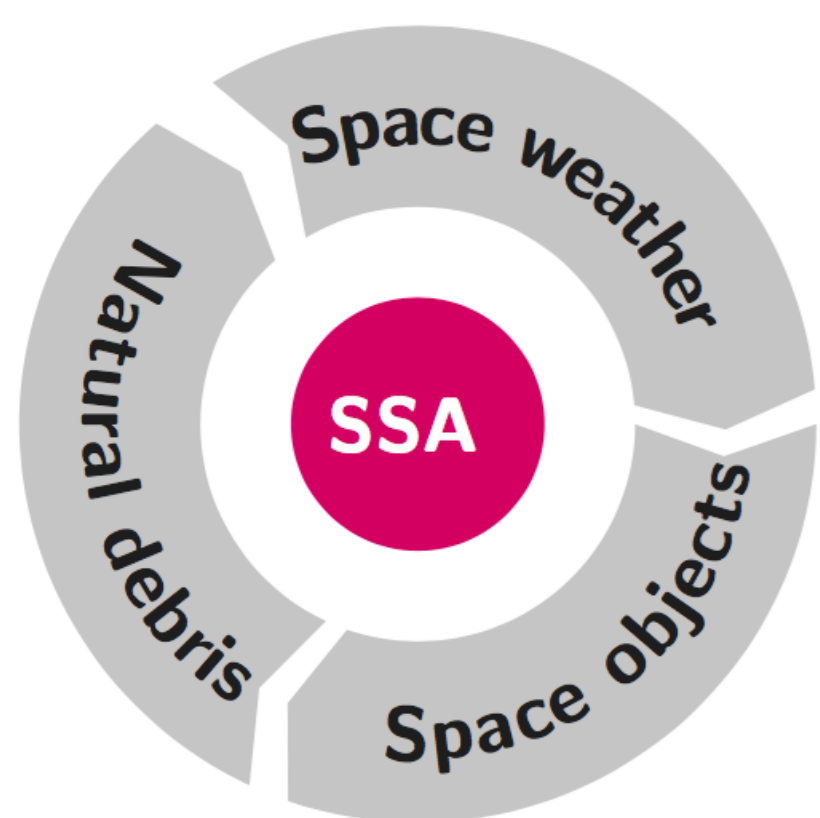## SPACE SITUATIONAL AWARENESS

Figure 1: SSA: the ability to view, understand and predict the physical location of objects in orbit around the Earth.

A prime requirement for the management of satellites, space-based services and technologies is to be able to precisely track and predict the orbit of satellites and any other objects in the environment. More than half of the total Earth-orbiting satellite population is in the 160–2000 km altitude range (LEO) with a commercial value in the order of hundreds of billion USD. The largest uncertainty in orbit tracking and prediction in the LEO region originates from the poor estimation of atmospheric drag. While many parameters contribute to atmospheric drag, in near-Earth space (160–800 km) the largest source of error is in the modelling of air density (atmospheric mass density, AMD). The modelling error of AMD is regarded to be around 15–20%. Reducing this error is an extremely important part in the development of new tools to improve the accuracy and reliability of orbit predictions.
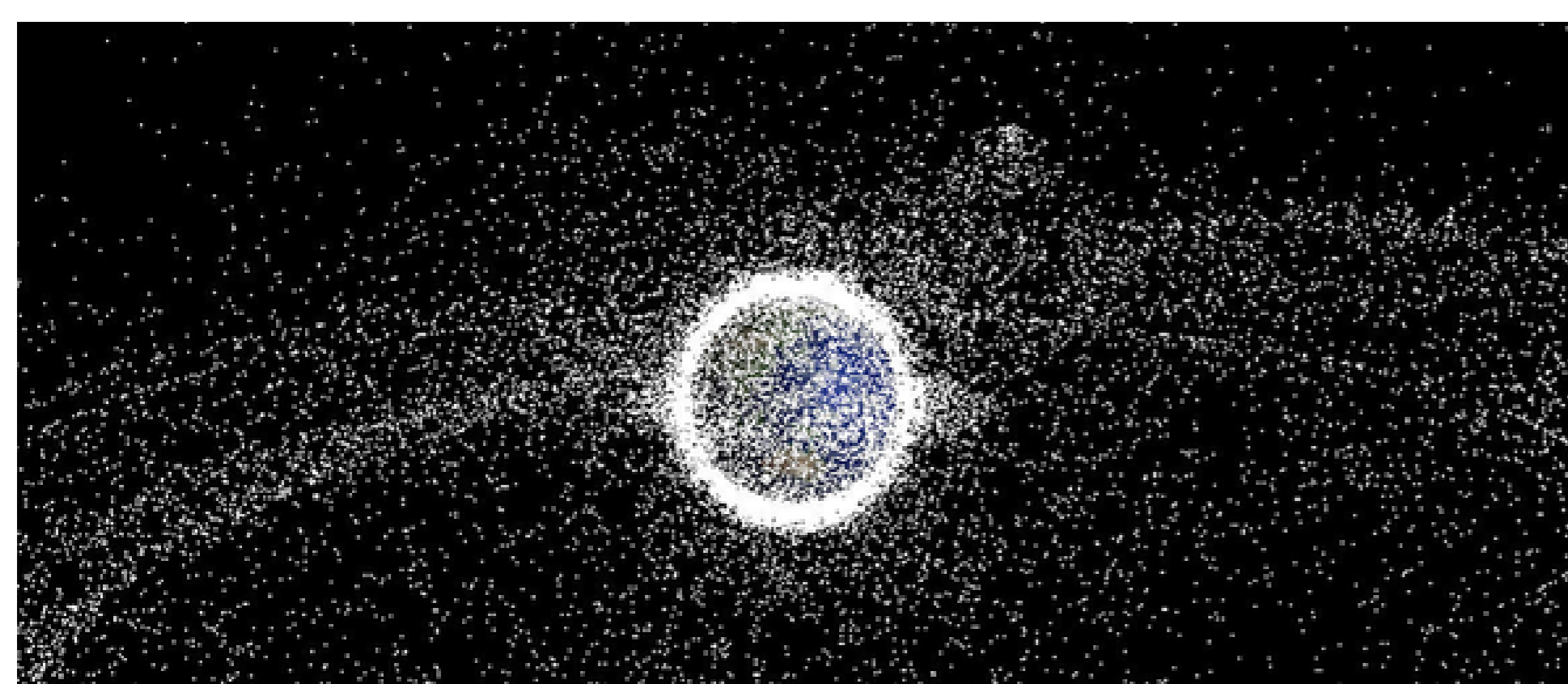

Figure 2: Illustration of the space debris population in near-Earth orbit. Image courtesy of University of Southampton, UK.
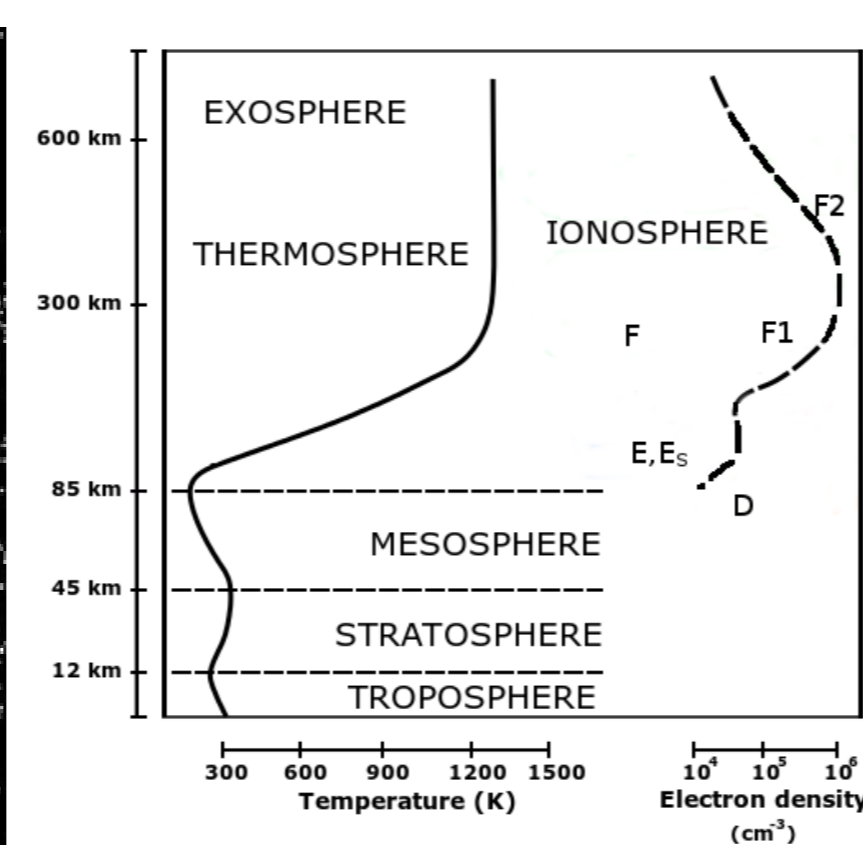

Figure 3: Illustration of the Earth's atmospheric layers.

ORBIT DETERMINATION AND ATMOSPHERIC MASS DENSITY

The largest error in predicting the orbit of a space object in LEO is the atmospheric drag due to modelling errors in the interaction between the object and its environment, and the AMD.

The AMD imparted drag acceleration $\mathbf{a_D}$ is described as

$$\mathbf{a_D} = -\frac{C_D A}{2\ m}\rho(\mathbf{V} - \mathbf{V_{atm}})^2 \left[\frac{\mathbf{V} - \mathbf{V_{atm}}}{|\mathbf{V} - \mathbf{V_{atm}}|}\right] \quad (1)$$

where:

C_D = drag coefficient for the atmospheric drag;
A/m = area-to-mass ratio;
ρ = AMD; and
$\mathbf{V}, \mathbf{V_{atm}}$ = object's velocity and local velocity of the atmosphere respectively.
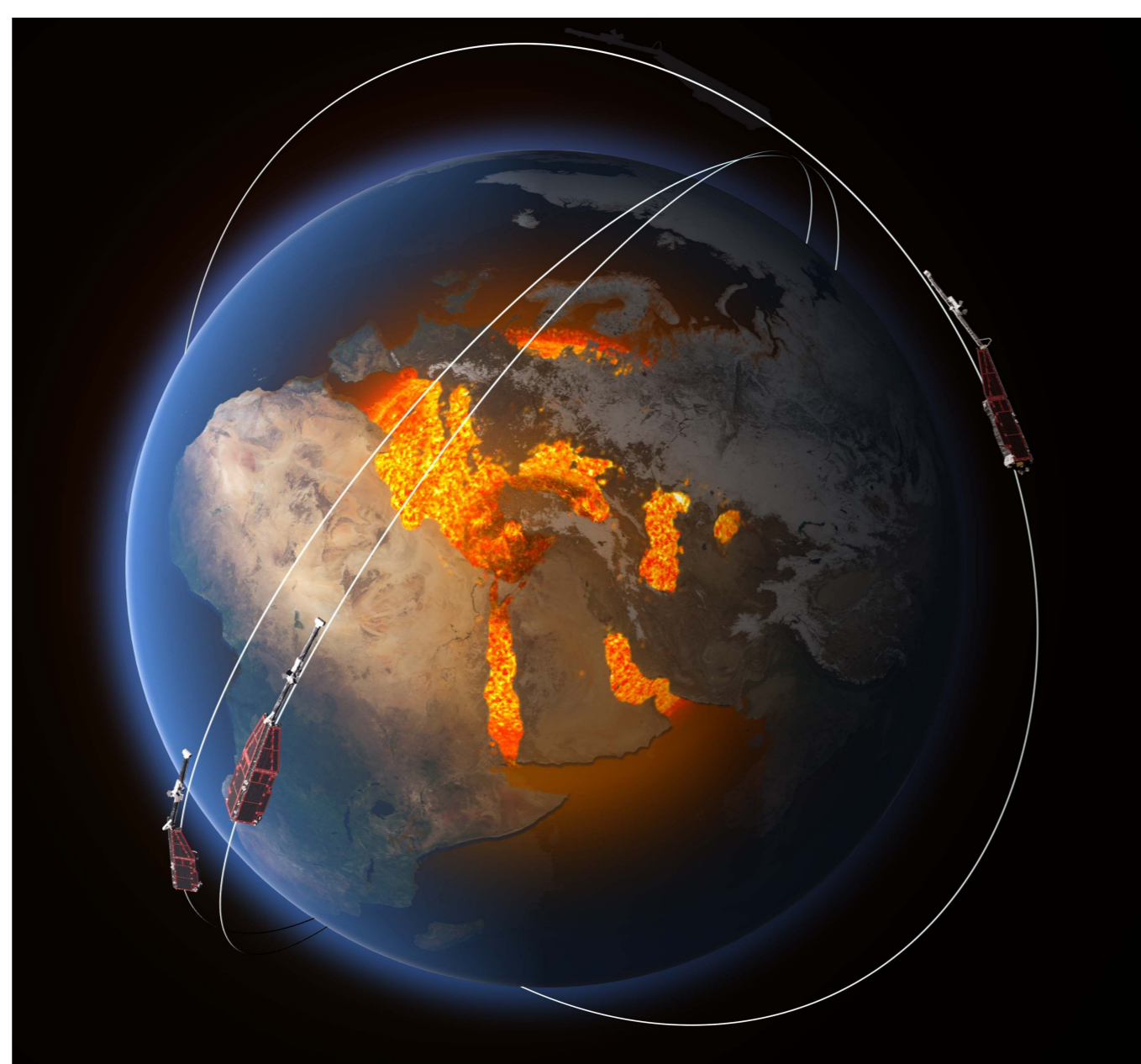

Figure 4: Swarm satellite constellation (average altitude, 480 km). Image courtesy of ESA/ATG Medialab.

MODELLING AMD IN A VARIABLE SPACE ENVIRONMENT

The coupling between the Earth's upper atmosphere and the space environment is far from well-understood. The atmosphere between 100 and 300 km altitude is too dense for long-life satellite observations but too thin for routine remote sensing, so modelling plays a key role in understanding this region. There are three main approaches to modelling the upper atmosphere: empirical, physics-based and data assimilation. Empirical models, although widely used, are unbefitting for nowcasting or forecasting as usually the relationship between model variables are determined via curve fitting techniques disregarding the underlying physical processes.
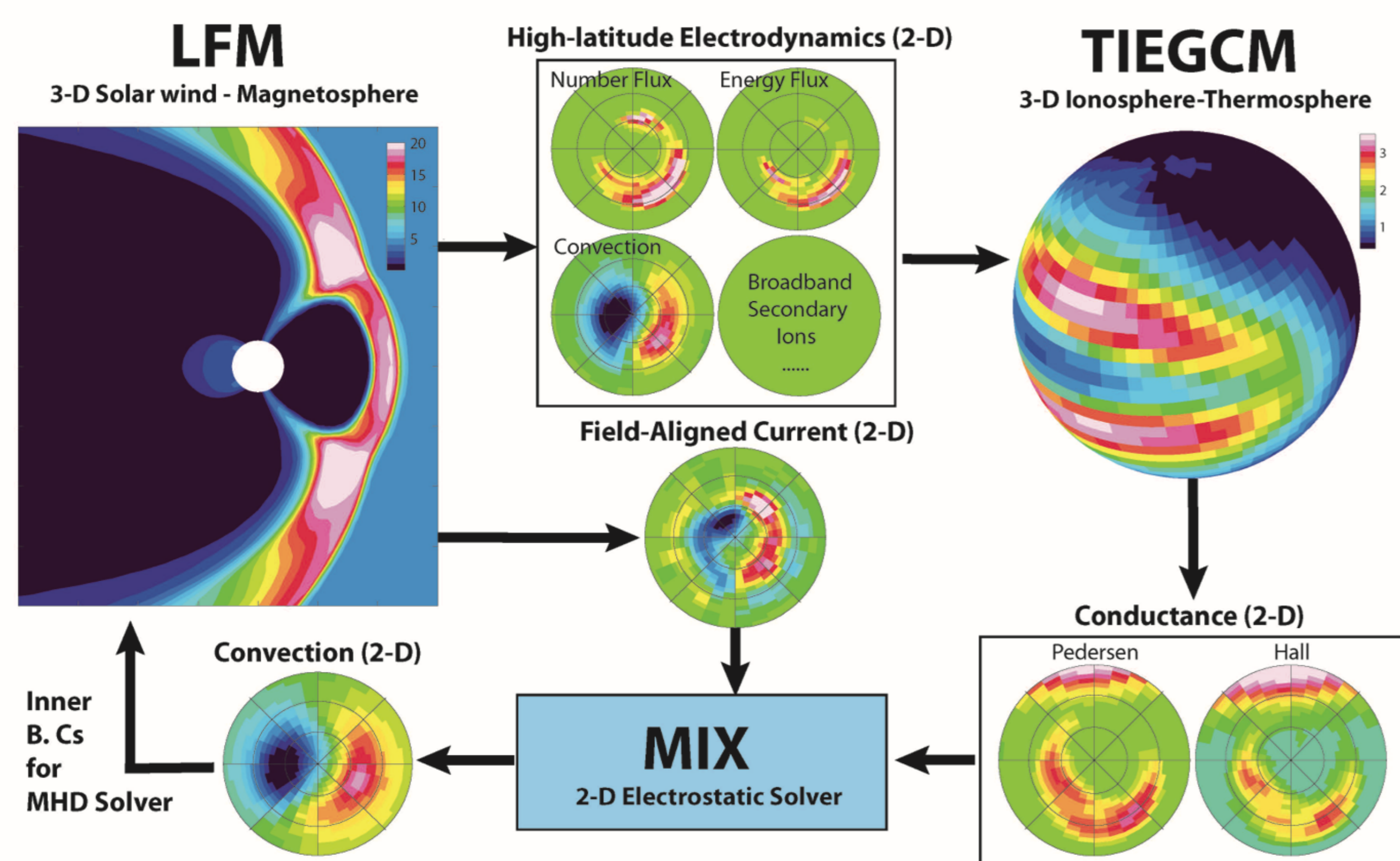

Figure 5: High-level illustration of some physical processes involved in quantifying the state of the coupled magnetosphere-upper atmosphere, which is an outstanding problem. Image courtesy of William Lotko, Dartmouth College.

Below, a study of the thermosphere using the physics-based Thermosphere-Ionosphere-Electrodynamics General Circulation Model (TIE-GCM) and observations from Swarm-C satellite is presented. Swarm, which was launched in late 2013, consists of three polar orbiting satellites (Fig. 4) designed for monitoring the magnetic field of the Earth. The measurements from on-board accelerometers and GPS receivers can be used to derive the in situ AMD.

RESULTS

First, the synchrony between the temperature and the AMD at higher altitudes during 1–31 July 2014 is examined.
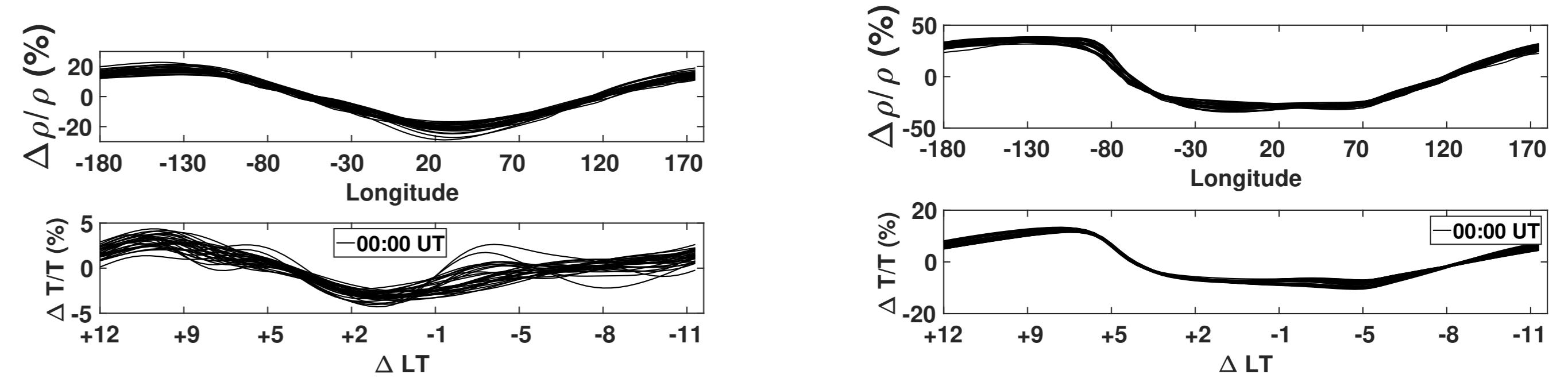

Figure 6: Simulation outputs of the relative deviation of AMD ($\Delta\rho/\rho$) at 400 km altitude (top row) and temperature ($\Delta T/T$) at 300 km altitude (bottom row) from the zonal mean during 1–31 July 2014 at 70° (left column) and 10° (right column) geographic latitude. The horizontal axes indicate the longitude and the corresponding local time (LT) specified as the difference to the given UT. Each line represents a day.
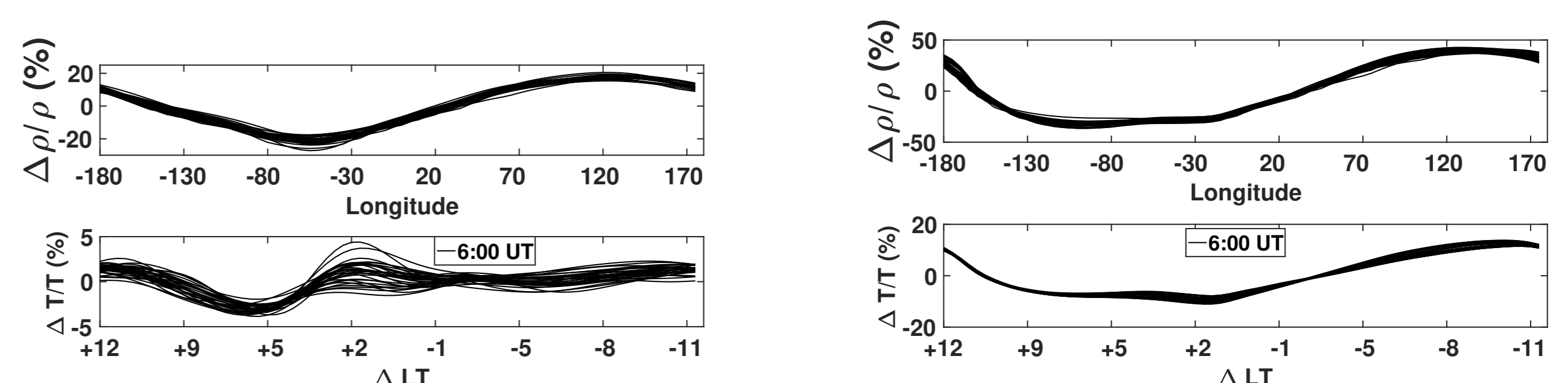

Figure 7: Same as Fig. 6 but for 06:00UT.

Figs. 6 and 7 display the synchrony between the AMD at 400 km altitude and the neutral temperature 100 km underneath for high-latitude and low-latitude regions. It can be seen that near the equator, the temperature variations are clearly synchronised with density 100 km above. A density–temperature synchrony is also apparent at high latitudes. However, the density peaks/troughs tend to be shifted towards the east compared to the temperature peaks/troughs. That is, for example, at 0 UT the density troughs close to 20°E have an apparent eastward shift of approximately 35° compared to the temperature troughs. Relative deviation of density and temperature in the high latitudes is also much more smaller as a percentage than near the equator. This result is important as it shows that variation in temperature underneath alone cannot fully explain the mass density structures seen in the high-latitudes. The morphology of thermospheric density in polar regions is complex and determining possible causes is an ongoing challenge.
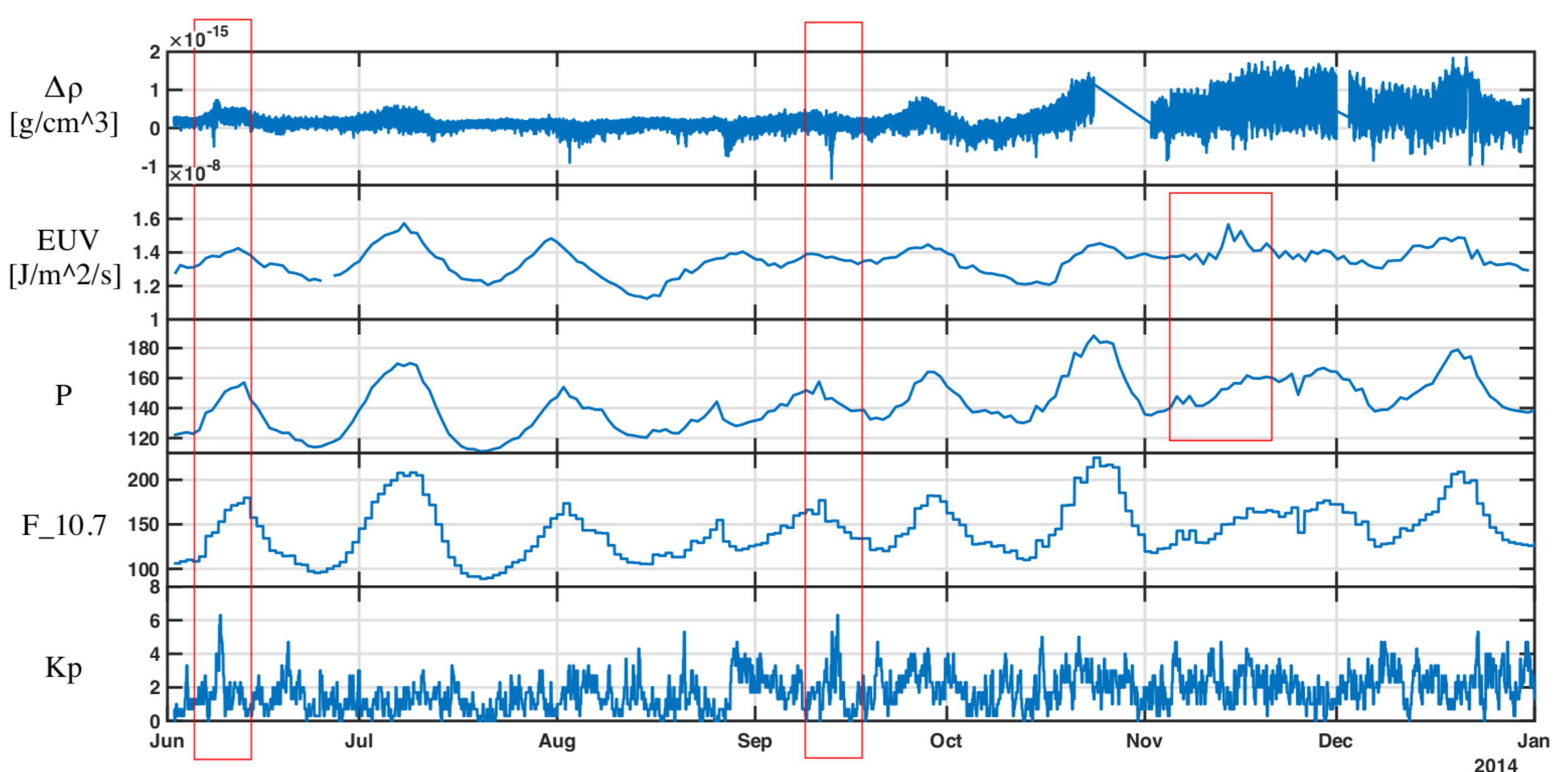

Figure 8: The difference between simulated and Swarm-C densities ($\Delta\rho$) compared against EUV flux observations, P solar index, $F_{10.7}$ solar flux and Kp index.

A striking resemblance between the distribution of difference in density ($\Delta\rho$) and space weather indicators is apparent in Fig. 8. TIE-GCM's capability to map the density along the Swarm-C orbit is shown in Fig. 9. It can be seen that simulated densities demonstrate reasonable correspondence with accelerometer-derived densities. Note the sharper spikes in Figs. 8 and 9 corresponding to times of increased geomagnetic and solar activity. The rapid drop in correlation in October can be attributed to the poor quality of Swarm data in that period.
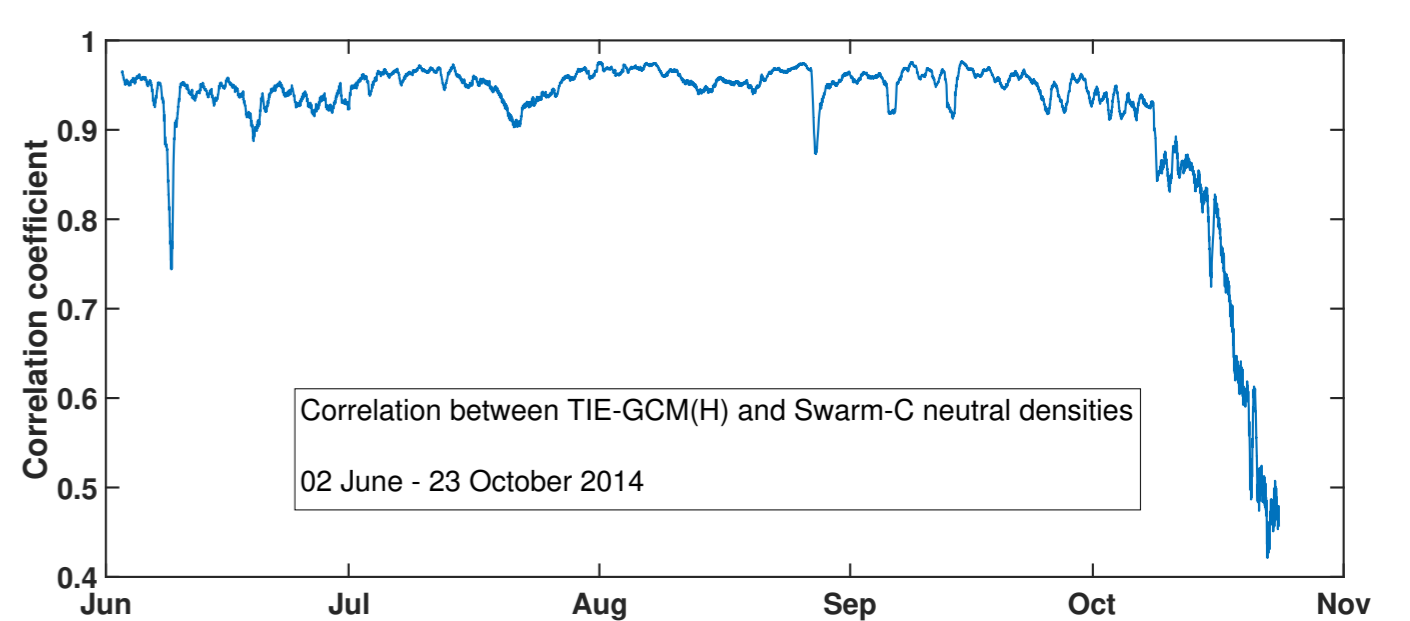

Figure 9: The daily correlation between simulated and accelerometer-derived mass densities. H indicates the Heelis ionosphere convection model.

TIE-GCM uses, among others, solar and geomagnetic proxies to determine the energy input to the thermosphere-ionosphere system. The P index, $0.5(F_{10.7} + 81$ day average $F_{10.7})$ was used in this study to define the solar input. However, these proxies do not fully characterise the solar and geomagnetic conditions, nor do they include any variations in forcing from the lower atmosphere (e.g. daily variability in tides/planetary waves).

CONCLUSIONS

We have shown that forcing caused by temperature from underneath on density above is a latitude dependent phenomenon, and at high-latitudes, such forcing may perhaps be subdued by other complex mechanisms. The eddy diffusion forced in the model is an ad hoc approximation; hence other lower atmospheric processes must be investigated further to quantify the contribution to change in thermospheric composition. The similitude between EUV flux and the difference in simulated and observed density indicates that the model's characterisation of the solar forcing needs improvement.